

## Large displacement numerical study of 3D plate anchors

This paper presents a numerical study carried out in the context of the development of a new application of plate anchors for landslide stabilization. The plates are positioned on the slope's ground surface and linked to a deeper stable layer with a steel grouted bar, thus acting as discontinuous elements constraining the slope movement. This technique is less expensive compared to standard retaining structures, especially in medium and deep landslides. Moreover, plate anchors can bear large displacements of the unstable moving mass without losing efficiency. Evaluating the stabilizing force and its optimization in relation to the plate shape are of great interest. Numerous studies have investigated the bearing capacity of rectangular and circular thin plates at small strains, but the performance of alternative shapes, such as cones or truncated cones, has never been considered. The numerical study here presented applies the Material Point Method to investigate the behaviour of plate anchors with different 3D shapes at large displacements. The numerical model is validated with the results of some small-scale laboratory tests. The pull-out resistance, the soil stress and displacement fields around the plate, and the group effect have been investigated, thus obtaining preliminary indications for the design of these elements.

Keywords: plate anchor; MPM; large displacements; landslide stabilization

*This is the accepted manuscript. The editorial version of the paper can be retrieved at: <http://www.tandfonline.com/doi/full/10.1080/19648189.2017.1408498>*

### 1 Introduction

Plate anchors are a particular type of earth anchors that develop a resistant force by means of a rigid element, i.e. a concrete, steel or timber plate or beam. This element is deeply embedded in the stable soil and linked to the external structure by a tie-rod. After installation, generally the tie-rod is put into tension to guarantee the stability of the system according to a designed safety factor.

Recently, plate anchors have been applied in an innovative passive reinforcement system to stabilize or reduce the displacement rate of slow-moving landslides (Cruden & Varnes, 1996). In this technique, the plate is placed on the ground surface or embedded

at a shallow depth and is connected to a deep stable layer by a fully grouted bar (Fig. 1). Like in the soil nailing technique, the anchors behave as passive reinforcements, i.e. no tension is applied to the bar and the reinforced system becomes active only when the slope movement develops. An important feature of this technique is that, if the slope is not completely stabilized and slowly deforms over time, large relative displacements between soil and plate will accumulate without significant loss of reinforcement efficiency. In fact, its stabilizing action remains active because it is ensured by the frictional resistance developed at the soil-plate interface (surface reinforcement) and along the bar at the soil-grout interface (global reinforcement). This feature is particularly interesting when the remedial works are implemented at different times, for instance, when the budget for the overall intervention is not available all at once.

Compared to standard rigid gravity walls or sheet pile walls, this innovative system has a lower cost, requires less time for installation and can be effectively used also for medium and deep slope movements (Bisson & Cola, 2014; Bisson, Cola, Tessari, & Floris, 2015).

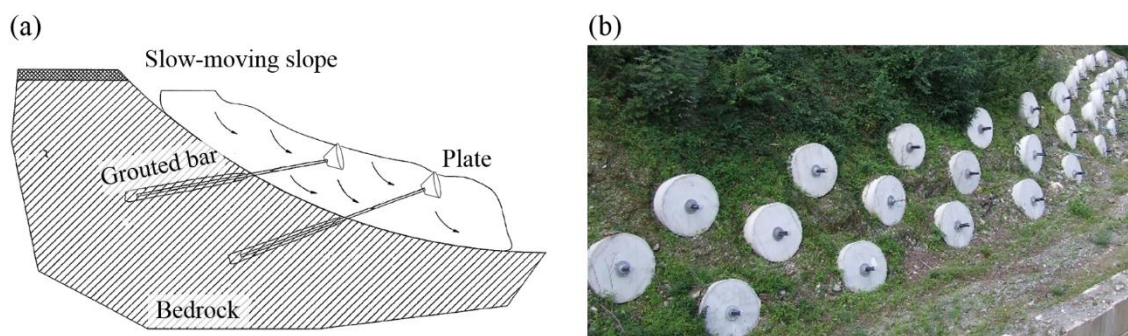


Figure 1 (a) schematic view of the use of plate anchors for slope stabilization and (b) example of application in Recoaro Terme (Italy)

For these applications, it is fundamental to assess the anchor resisting mechanism at large displacements, and the punching pressure. Moreover, experience suggests that the use of 3D shapes such as cones or pyramids for the plate seems efficient. Intuitively the behaviour of 3D shapes differs from the one of thin plates, but to the authors'

knowledge, this aspect has never been investigated in detail. The aim of this paper is to study numerically the behaviour of 3D plate anchors considering large displacements and shape effects.

A number of theoretical and experimental studies investigated the pull-out resistance of horizontal anchors with vertical thin plates embedded in cohesion-less or cohesive soils (e.g. Das, 2013; Merifield & Sloan, 2006) and developing relatively small displacements. These studies permitted the evaluation of the importance of some geometrical factors, such as the embedment ratio, the width of the plate and the spacing between anchors in groups. However, only strip, thin square and circular plates have been considered.

Since the large soil-plate displacements cannot be captured with the standard Lagrangian FEM because of issues with element distortions, Arbitrary Lagrangian–Eulerian methods (ALE) and particle-based methods have been developed in the last few decades (Atluri & Zhu, 2000; Donea & Huerta, 2004). Among them, the remeshing and interpolation technique with small strain (RITSS) method (Hu & Randolph, 1998), the coupled Eulerian–Lagrangian (CEL) method (Grabe, Qiu, & Wu, 2015; Qiu, Henke, & Grabe, 2011), and the Material Point Method (MPM) (Sulsky, Chen, & Schreyer, 1994) have been successfully applied in soil penetration problems similar to the anchor pull out discussed in this paper (F Ceccato, Beuth, & Simonini, 2016; Mahmoodzadeh & Randolph, 2014; Phuong, van Tol, Elkadi, & Rohe, 2016; Qiu & Grabe, 2011; Qiu & Henke, 2011; Tian, Cassidy, Randolph, Wang, & Gaudin, 2014).

RITSS method is essentially a form of ALE with small strain Lagrangian calculations in each incremental step and ‘convection’ of stresses and material properties from the old mesh to the new mesh. A drawback of the method is the computational cost of mesh regeneration with structures of complex geometries and the inaccuracies

introduced during mapping of quantities to the new mesh. In the CEL analysis, the soil is modelled as an Eulerian material that flows through a fix mesh, while the structure is modelled as a Lagrangian material (Noh, 1994). The soil-structure constraints are enforced with a contact algorithm usually based on the penalty method (Qiu et al., 2011).

This study applies the MPM, which is a continuum-based particle method that simulates large displacements by means of Lagrangian material points (MP) moving through an Eulerian grid (Sulsky, Zhou, & Schreyer, 1995). The MP carry all the information of the continuum; in contrast, the computational grid does not store any permanent information and can be redefined at the end of each time step. A brief description of the method can be found in Appendix A.

The numerical analyses are performed using the dynamic explicit code Anura3D ([www.anura3d.eu](http://www.anura3d.eu)), which implements a full 3D MPM formulation and it is therefore suitable to simulate the three-dimensional soil deformations induced by the movement of the plate. It implements an enhanced version of the original MPM proposed by Sulsky, Chen, & Schreyer, (1994), which has been extensively validated for geomechanical problems (Al-Kafaji, 2013; Fern et al., 2016; Yerro, 2015) including slope failures (Soga, Alonso, Yerro, Kumar, & Bandara, 2016; Yerro, Alonso, & Pinyol, 2016) and soil penetration problems (Ceccato et al., 2016; Ceccato, Beuth, Vermeer, & Simonini, 2016; Phuong et al., 2016).

The software features a contact formulation (Al-Kafaji, 2013; Ceccato, 2014; Ceccato, Beuth, & Simonini, 2017), based on the algorithm originally proposed by Bardenhagen et al. (2001), which can model the soil-plate frictional contact (Appendix B).

Dry soil is considered in this study, thus the one-phase formulation is applied and the behaviour of soil is simulated with an elastoplastic model with Mohr-Coulomb failure criterion.

The numerical model (Sec. 3) has been validated considering a set of small-scale laboratory pull-out tests performed at the University of Padua (A. Bisson, 2014). In these tests, the pull-out force for different plate shapes is measured as function of anchor displacement as explained in Section 2.

The results of the numerical simulations are presented in Section 4. The MPM model has been exploited to study some aspects that could not be fully investigated in the physical model, such as geometry and size of the three-dimensional volume of soil heavily influenced by anchor presence, the effect of spacing when anchors are used in-group, and the effect of soil friction angle. Based on these numerical results, it has been possible to draw preliminary guidelines for the design of isolated and in group plate anchors.

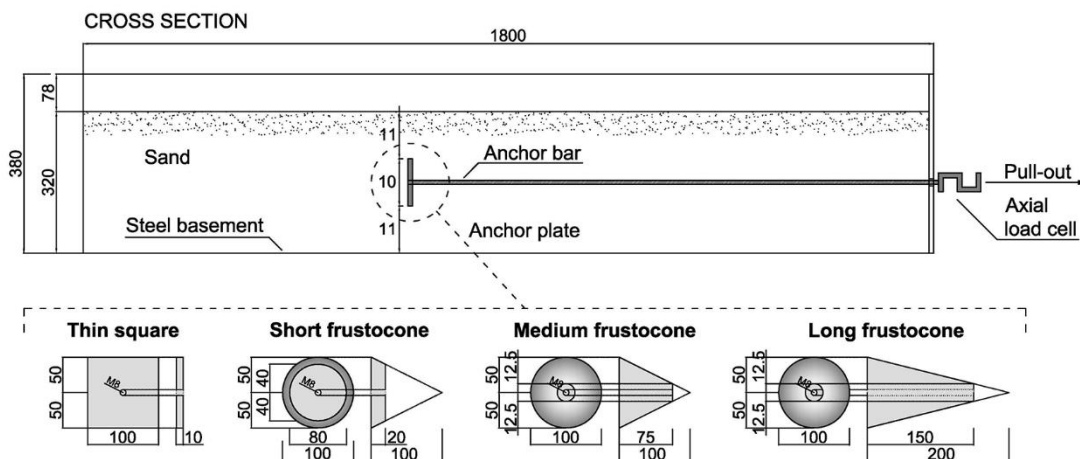


Figure 2 Physical model scheme and geometry of the plate anchors used in the pull-out tests (dimensions in millimetres)

## 2 Laboratory experiments

A small-scale physical model (Fig. 2) in normal gravity conditions has been set up. The model consists of a parallelepiped box and it is 180 cm long, 45 cm high and 40 cm wide.

The bottom boundary of the model is made rough by gluing sand grains on the surface. Two transparent glasses, 3 cm thick, are used for the side walls, thus allowing the observation of the displacement field during loading by means of image processing techniques such as PIV (Adrian, 1991; White, Take, & Bolton, 2003) and image difference (Rosin & Ellis, 1995). A Canon EOS 400D digital camera, with 10.1 megapixel CMOS sensor and ultra-wide angle lens EFS 10-22 mm is placed in a lateral position, 60 cm distant from the glass, and takes a picture every 5 seconds during the loading test.

The box is filled with dry sand by in-air pluviation and inside hosts the plates. The relative density is 87% and the dry unit weight  $16.05 \text{ kN/m}^3$ . A medium-fine quartz sand from the Adige river has been used in the physical model, with mean particle size  $D_{50} = 0.42 \text{ mm}$ , coefficient of uniformity  $U = D_{60}/D_{10} = 2.0$ , specific density of the grains  $G_s = 2.71$ , minimum and maximum dry unit weight  $\gamma_{d,\min} = 13.6 \text{ kN/m}^3$  and  $\gamma_{d,\max} = 16.5 \text{ kN/m}^3$  (Gottardi & Simonini, 2003). The sand resistance parameters are known from previously conducted experimental tests (Gabrieli, Cola, & Calvetti, 2009; Simonini, 1987, 1996). The peak friction angle, determined by direct shear test, is between  $44.3^\circ$  and  $40.6^\circ$  depending on the relative density and the vertical stress, while the critical state friction angle is  $35.5^\circ$ .

Four aluminium shapes have been used for the anchor plate (Fig. 2):

- (1) Thin square plate anchor (TS): square prism 100x100 mm, 10 mm thick;
- (2) Short frustoconical plate anchor (SFC): truncated cone, major base diameter 100 mm, smaller base diameter 80 mm, 20 mm thick;
- (3) Medium-long frustoconical plate anchor (MFC): truncated cone, major base diameter 100 mm, smaller base diameter 25 mm, 75 mm thick

- (4) Long frustoconical plate anchor (LFC): truncated circular cone, major base diameter 100 mm, smaller base diameter 25 mm, 150 mm thick.

The plate's lateral surface is covered with glued sand, providing a rough frictional interface. The thickness of the sand layer in the box is 32 cm and the plate is positioned in the middle. The embedment ratio ( $H/B$ ) is 1.6, where  $H=16$  cm is the depth of embedment, i.e. the vertical distance between the soil surface and the base of the plate, and  $B=10$  cm is the plate's characteristic width.

The plate is linked with a bar to the pull-out system, placed externally at the end of the box (Fig. 3). The system moves the plate horizontally at the slow rate of 10 mm/min, which prevents dynamic effects. A load cell is placed between the bar and the extractor to measure the axial pull-out force with time.

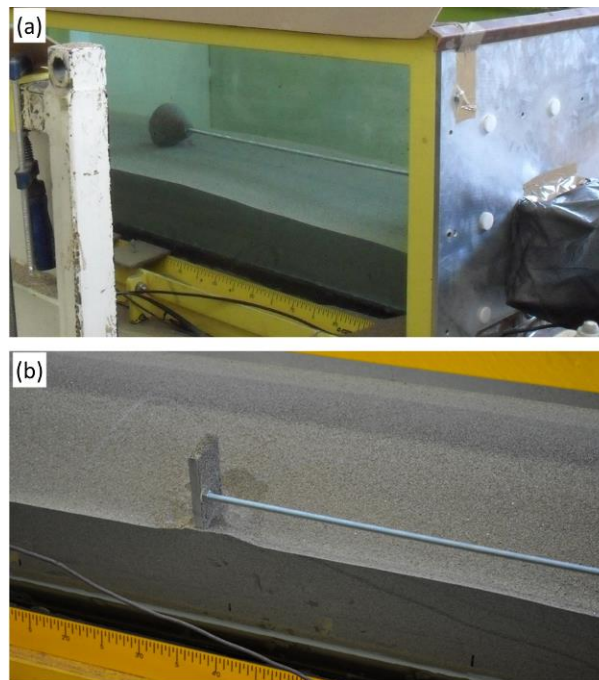


Figure 3 Preparation of the physical model: (a) central position of the plate (test set A) and (b) lateral position of the plate (test set B).

Two series of tests have been performed: the first aimed at measuring the pull-out resistance of the plates embedded in the centre of the box (test set A, Fig. 3a); the second aimed at assessing the soil displacement field around the plate (test set B, Fig. 3b). In the

latter, half-sectioned plates leaning on a lateral glass wall were considered. Assuming a negligible soil-glass friction, the glass represents a symmetry plane and therefore the observed soil motion is similar to the motion along the median vertical plane of the full sized plate anchors used in test set A. Figure 3 shows two pictures taken during the preparation of the tests where the position of the plate during test set A and test set B can be visualized. For a full discussion of the experimental tests, results and PIV analysis, please refer to A. Bisson (2014).

With the progressive movement of the anchor, an active wedge develops at the back of the plate, forming a funnel shape at the surface, while the soil in front of the anchor is gradually compressed and pushed upwards.

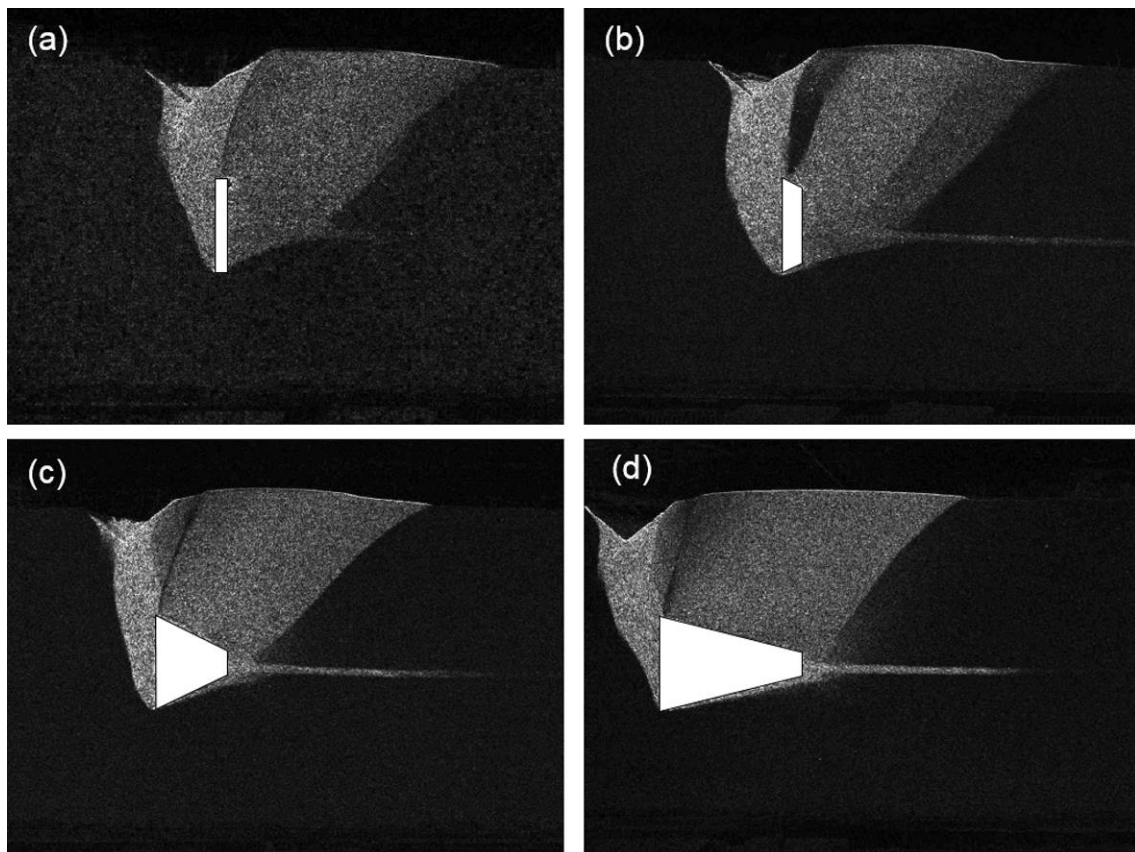


Figure 4 Absolute image difference for a plate displacement between 50.00mm and 50.83mm during test set B; (a) TS, (b) SFC, (c) MFC and (d) LFC.

Figure 4 shows the absolute image difference between two subsequent frames after a plate displacement of 50 mm (test set B). The technique consists in converting the pictures in

greyscale; then the grey values of each pixel in one image are subtracted with the corresponding values in the previous frame. This method provides an image with light pixels in the zones that have experienced movements, and dark pixels in the static zones, thus allowing to evaluate the static and moving areas. The displacement magnitude and direction cannot be deduced with this technique.

In each experiment, the anchor resistance increases with displacement reaching a peak value after a few millimetres, then it decreases and remains approximately constant at large displacements. As mentioned in the introduction, the main application of these 3D plate anchors is slope stabilization, where large relative movements between the soil and the plate are expected. For this reason, this paper focuses on the effect of plate shape on the resistance at large displacements.

The considered pull-out resistance refers to test set A and it is the ratio between the pull-out force at large displacements and the area ( $A$ ) of the anchor projected in a plane perpendicular to the direction of movement, i.e.  $A=B^2$  for the TS and  $A=\pi B^2/4$  for SFC, MSF and LFC ( $B$  = size of the anchor = 100 mm). The thin square plate exhibits the minimum pull-out resistance (47.4 kPa), followed by the short frustocone (54.3 kPa), the medium frustocone (66.2 kPa) and the long frustocone (71.8 kPa).

### **3 The numerical model**

We can assume that the experimental model has a vertical symmetry plane passing through the symmetry axis of the anchor. Taking advantage of this symmetry, only a half-width of the laboratory experiment is simulated. The soil domain is 110 cm long, 20 cm wide and 32 cm high (Fig. 5a). Note that, in order to reduce the computational cost, the length of the numerical model is shorter than the true size of the laboratory model. Preliminary analyses considered  $L=50$  cm, 80 cm, 110 cm and 120 cm allowing us to conclude that with a length of 110 cm the boundaries are far enough to avoid any

influence on the results.

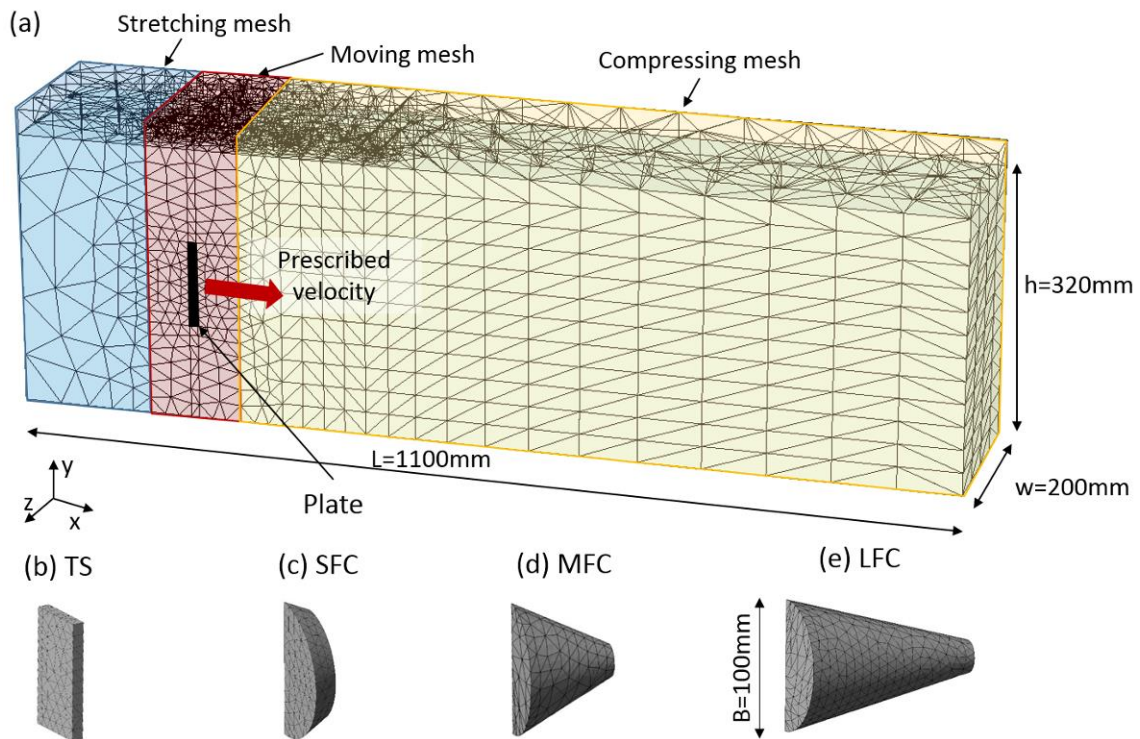


Figure 5 Geometry and discretization of the MPM model (dimensions in millimetres)

Like in FEM, also with MPM a proper definition of the domain discretization is fundamental for reducing the mesh-dependency of the results (Francesca Ceccato & Simonini, 2016; Fern & Soga, 2016; Kumar Soundararajan, 2015). The optimal geometry and discretization of the model have been determined through preliminary analyses, which are not reported here for the sake of brevity. The mesh is finer near the plate, where higher stresses and deformation gradients are expected. The size of the tetrahedral elements discretizing the plate is about 8 mm (Fig. 5b-d). 20 MPs are initially located inside each element close to the anchor, while 10 or 4 MPs fill the elements further away. A volume of initially empty elements overlays the top surface of the soil in order to accommodate vertical displacements of the MPs induced by the anchor movement.

Roller boundary conditions are applied at the lateral surfaces while the bottom boundary is fully fixed. These conditions mimic the smooth glass surfaces and the very rough bottom of the physical model. The plate is much stiffer than the surrounding soil,

thus it is assumed to behave as a rigid body, which moves horizontally by a prescribed velocity ( $v$ ) applied at the MPs of the structure.

In order to reduce the computational cost, the plate velocity adopted in the numerical model is 20 mm/s, which is higher than the 0.17 mm/s used in the experiment, but sufficiently slow to avoid the dynamic effects which can give oscillations on the measured anchor resistance. Figure 6 shows the evolution of the TS resistance with displacement for different values of  $v$ . The applied velocity does not significantly influence the limit resistance of the anchor because strain-rate dependency of the material behaviour is not considered. However, oscillations due to dynamic effects appear for  $v = 200$  mm/s, thus a value of 20 mm/s is considered appropriate for this problem.

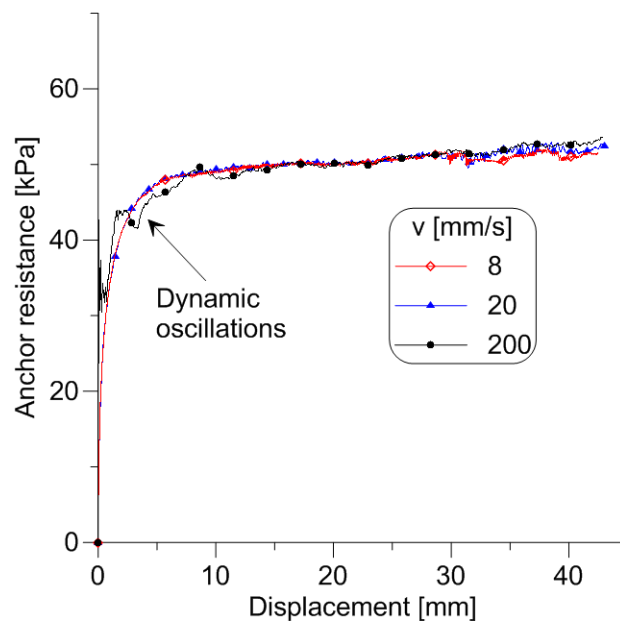


Figure 6 Resistance of the TS plate for different values of the anchor velocity

The contact between the soil and the plate is modelled by the multi-velocity field contact algorithm proposed by Bardenhagen et al. (2001) as implemented in the software *Anura3D* (Al-Kafaji, 2013; Ceccato et al., 2017). In this approach, the contact is solved at the nodal level; the velocities at the nodes of the contact surface are predicted from the solution of each body separately and then corrected imposing the impenetrability condition and the Coulomb's friction criterion. A brief description of the algorithm can

be found in Appendix B. In these simulations, a friction coefficient  $\mu$  equal to the tangent of the friction angle of the sand characterizes the soil-plate interface.

In order to keep the fine mesh always around the plate, a moving mesh approach is applied (Beuth, 2012; Ceccato et al., 2016; Phuong et al., 2016). It consists in adjusting the mesh with the movement of the plate. A fixed mesh region next to the plate moves with the same displacement as the anchor, while the compressed mesh in front of the plate and the stretched mesh behind the plate deform accordingly (Fig. 5a).

The use of the moving mesh approach is particularly convenient in combination with the contact algorithm because the contact nodes and the normal vectors to the contact surface do not change through the computation, thus improving the efficiency and accuracy of the simulation.

The constitutive response of sand is modelled with a linear elastic, perfectly plastic model with Mohr-Coulomb failure criterion. The input parameters are summarized in Table 1. Since the goal of the numerical simulations is to study the behaviour of the plate at large displacements, the dilatancy and the cohesion are equal to zero and the friction angle corresponds to the critical state friction angle. This model offers a simplified description of sand behaviour. Indeed, if one neglects soil dilatancy and strain-softening response, the peak condition followed by material softening, observed in the experiment, cannot be captured. However, the results at large displacements are considered representative of the post-peak conditions.

Stresses are initialized applying the so-called K0 procedure: vertical stresses initially assume a lithostatic distribution ( $\sigma'_{v0} = (1 - n)\rho_s g y_d$   $y_d$ =depth of the considered point) and horizontal stresses are computed as  $\sigma'_{h0} = K_0 \sigma'_{v0}$ , where  $K_0$  is listed in Table 1.

The plate resistance is calculated as the sum of the nodal horizontal forces on the soil-plate interface divided by the projected area.

Table 1 Material parameters for the numerical model

Parameter	Symbol	Value
Young modulus [MPa]	E	12
Poisson ratio [-]	$\nu$	0.2
Solid grain density [kg/m <sup>3</sup> ]	$\rho_s$	2650
Cohesion [kPa]	c	0
Friction angle [°]	$\phi$	35.5
Dilatancy angle [°]	$\psi$	0
Earth pressure coefficient	$K_0$	0.426
Porosity	n	0.4

## 4 Numerical results

### 4.1 Anchor resistance

Figure 7 shows the anchor resistance vs displacement curves obtained for the tested shapes. The anchor resistance increases with the displacement approaching monotonically the limit resistance ( $q_{lim}$ ). This behaviour is a consequence of the use of a linear-elastic perfectly-plastic model. The displacement-resistance curve shows small numerical oscillations probably due to the explicit time integration scheme and the grid-crossing errors which affect MPM (Steffen, Kirby, & Berzins, 2008). However, it can be well fitted by a hyperbole, whose horizontal asymptote is assumed to coincide with the limit resistance (Das & Seely, 1975). After a displacement of approximately 30 mm the resistance is about 98%  $q_{lim}$ . The simulation is carried up to the clear development of the limit resistance, i.e. about 50 mm.

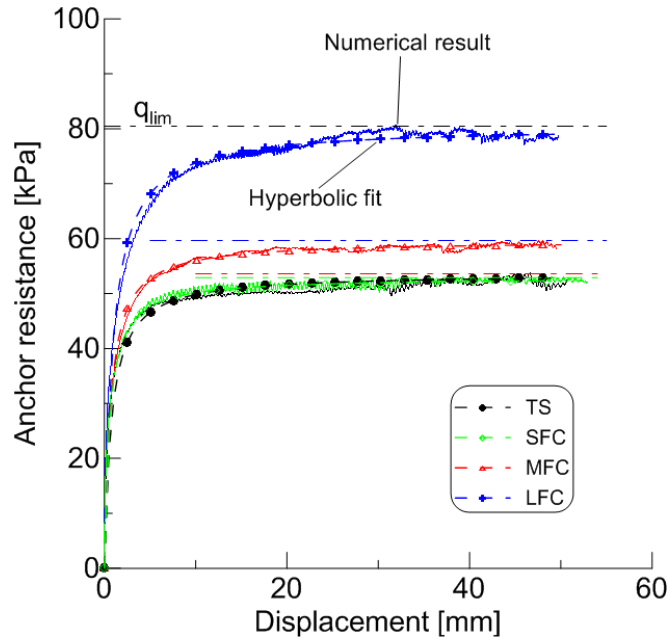


Figure 7 Anchor resistance over displacement for different anchor shapes

Table 2 Anchor resistance for different shapes

Shape		Numerical	Experimental	Difference	Shape factor
		$q_{lim}$ [kPa]	$q_{exp}$ [kPa]	$(q_{lim} - q_{exp})/q_{exp}$ [-]	$q_{lim}/q_{lim,TS}$ [-]
Thin square	TS	53.6	47.4	13%	1.00
Short frustocone	SFC	52.9	54.3	-2.5%	0.99
Medium frustocone	MFC	59.7	66.2	-9.8%	1.11
Long frustocone	LFC	80.4	71.8	11.9%	1.50

The long frustocone is the shape that offers the highest resistance (71.8 kPa), followed by the medium frustocone (66.2 kPa). The thin square plate and the short frustocone have approximately the same resistance. This result is explained by the fact that a larger volume of soil near the plate contributes to the development of the resistance of LFC and MFC, as better explained in Section 4.2, and they have a larger lateral surface, compared to TS and SFC, over which shear resistance is mobilized.

The numerical estimate of the limit resistance  $q_{lim}$  is in good agreement with the experimental post-peak resistance  $q_{exp}$  (Tab. 2). The difference between  $q_{lim}$  and  $q_{exp}$  is between 2.5% and 13%, which is assumed acceptable when considering the experimental inaccuracies and the model simplifications. Moreover, it should be noted that no

calibration of the material parameters was performed with the purpose of fitting the experimental results. This means that the essential features of the problem are relatively well captured by the numerical model.

The resistance of thin plate vertical anchors in cohesionless soils has been investigated in many published works, and a number of expressions to estimate the bearing capacity has been proposed (B. Das, 2013). In order to extend these results to plates of different shapes, we introduce a shape factor  $S_f$  that represents the ratio between the limit capacity of the frustoconical shape and the limit capacity of the thin square plate. The last column of Table 2 summarizes the shape factors derived from the numerical results. Note that  $S_f=1.50$  for the LFC, which means that this elongated shape produces an increment of 50% in the resistance if compared to a TS of the same size.

In practical applications, the shape factor may allow the estimate of the limit resistance of the frustoconical anchor from the limit resistance of the thin plate ( $q_{lim,TS}$ ), computed by one of the methods proposed in literature (e.g. B. Das, 1975; Neely, Stuart, & Graham, 1973; Ovesen, N. K. & Stromann, 1972):

$$q_{lim} = S_f q_{lim,TS} \quad (1)$$

#### **4.2 Stress and displacement fields**

One of the advantages of the 3D MPM simulations is the possibility to investigate the stress and displacement fields more easily than with the experiments, thus estimating the volume of soil significantly influenced by the anchor movement.

Figure 8 shows the horizontal stress in a horizontal section crossing the mid-plane of the anchor; it refers to a displacement of the plate of 50 mm, at which the pull-out capacity is fully mobilized. The initial horizontal stress in the considered cross section is 1 kPa. Dotted lines highlight the effective stress equal to 5 kPa. This value is approximately 10%

of the bearing capacity of the TS and it is taken as a reference for a qualitative estimate of the dimensions of the pressure bulbs for each shape.

The geometry and size of the pressure bulbs are strongly influenced by the shape of the plate. LFC has the widest area subjected to a horizontal stress greater than 5 kPa, followed by MFC, TS and SFC. The extension of the pressure bulbs in  $z$  direction is between 1.2 and 1.5D, except for LFC for which it hits the model boundary.

Figures 9 and 10 show the total displacement field in a vertical and a horizontal section through the centre of the plate for an anchor displacement of 50 mm. The dotted lines mark a displacement of 5 mm, which corresponds to 10% of the anchor displacement. The soil moves upward in front of the anchor and downward in the back, which generate respectively heave and settlement of the soil surface. This movement of the soil near the plate is qualitatively similar to the movement observed in the laboratory test set B (Fig. 4).

Table 3 Numerical mobilized areas in front ( $A_F$ ) and behind ( $A_B$ ) the anchor plate ( $A$ =plate rear base surface)

Shape	Horizontal cross section			Vertical cross section		
	$A_F$ [mm <sup>2</sup> ]	$A_B$ [mm <sup>2</sup> ]	$(A_F - A_B)_h/A$ [-]	$A_F$ [mm <sup>2</sup> ]	$A_B$ [mm <sup>2</sup> ]	$(A_F - A_B)_v/A$ [-]
Thin square	126.4	36.8	0.0090	485.5	184.5	0.0301
Short frustocone	96.5	33.7	0.0080	407.1	182.2	0.0286
Medium frustocone	122.6	29.9	0.0118	426.9	166.1	0.0332
Long frustocone	172.4	24.0	0.0189	565.8	169.5	0.0505

Table 4 Mobilization factors estimated from the horizontal ( $r_{mh}$ ) and vertical ( $r_{mv}$ ) cross sections

Shape	Numerical		Experimental (Bisson, 2014)
	$r_{mh}$ [-]	$r_{mv}$ [-]	$r_{mv}$ [-]
Thin square	1.00	1.00	1.00
Short frustocone	0.89	0.95	1.02
Medium frustocone	1.32	1.10	1.28
Long frustocone	2.11	1.68	1.71

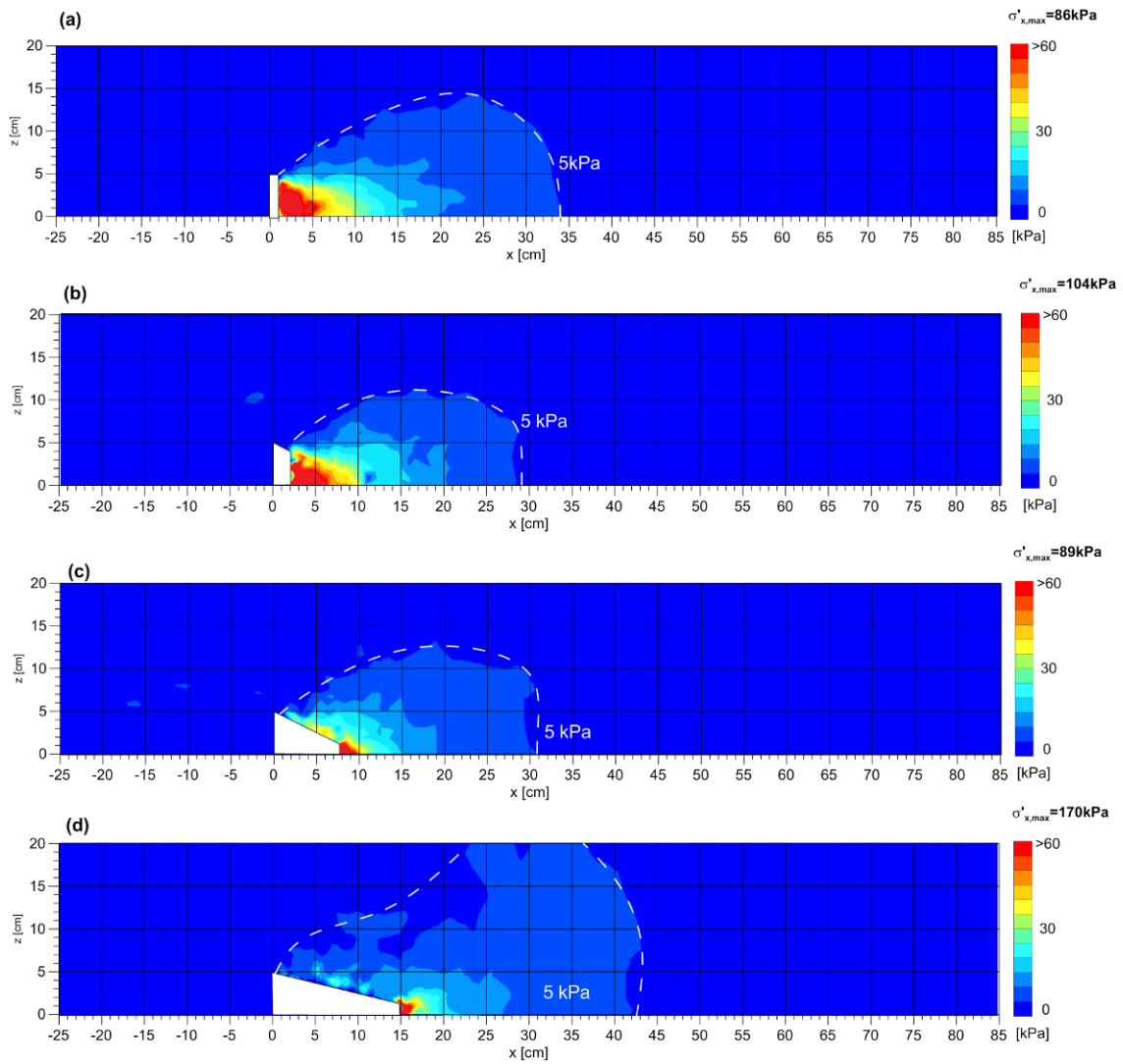


Figure 8 Horizontal effective stress in a horizontal cross section through the middle of the plate anchor: (a) TS, (b) SFC, (c) MFC, (d) LFC.

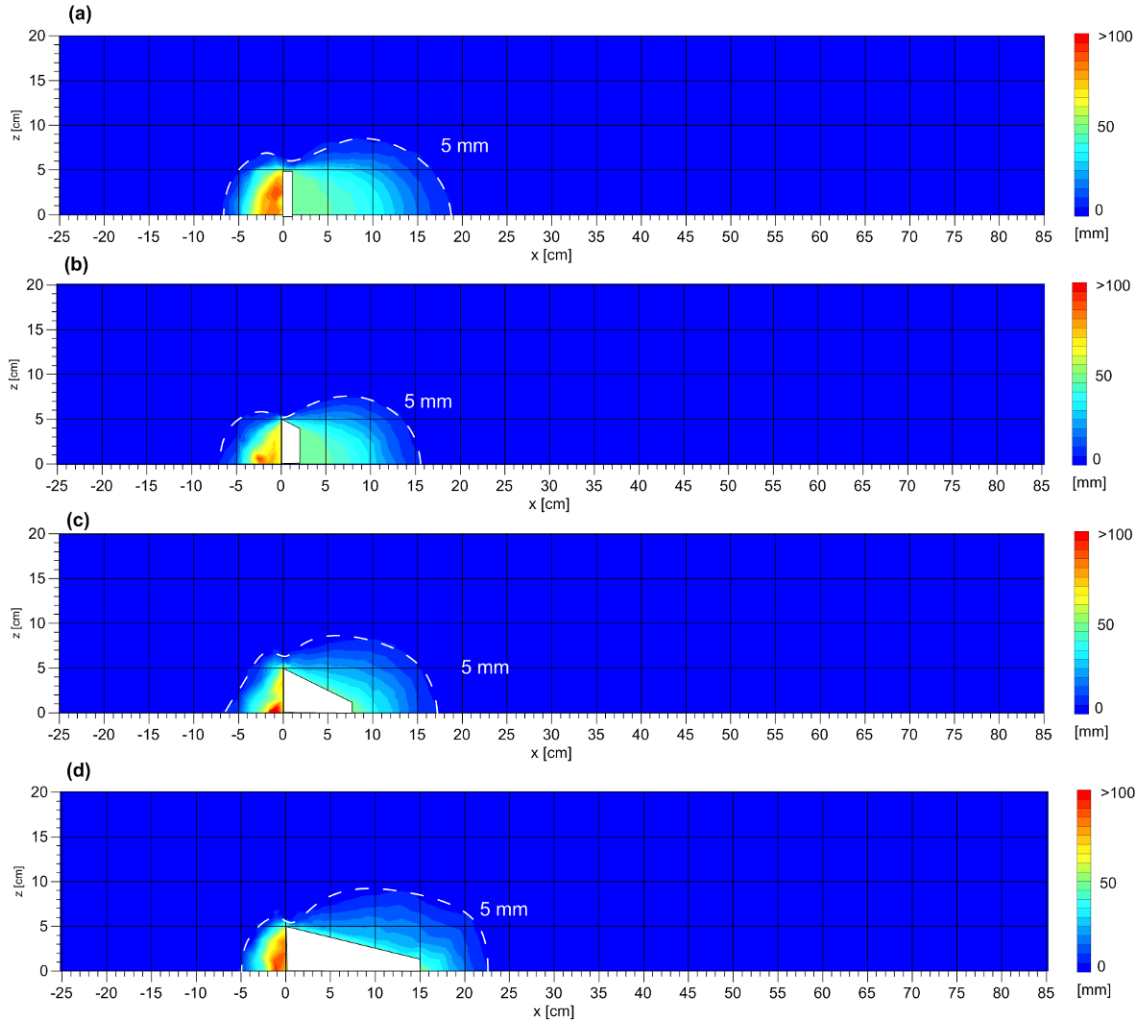


Figure 9 Total displacements in a horizontal cross section through the middle of the plate anchor: (a) TS (b) SFC, (c) MFC, (d) LFC

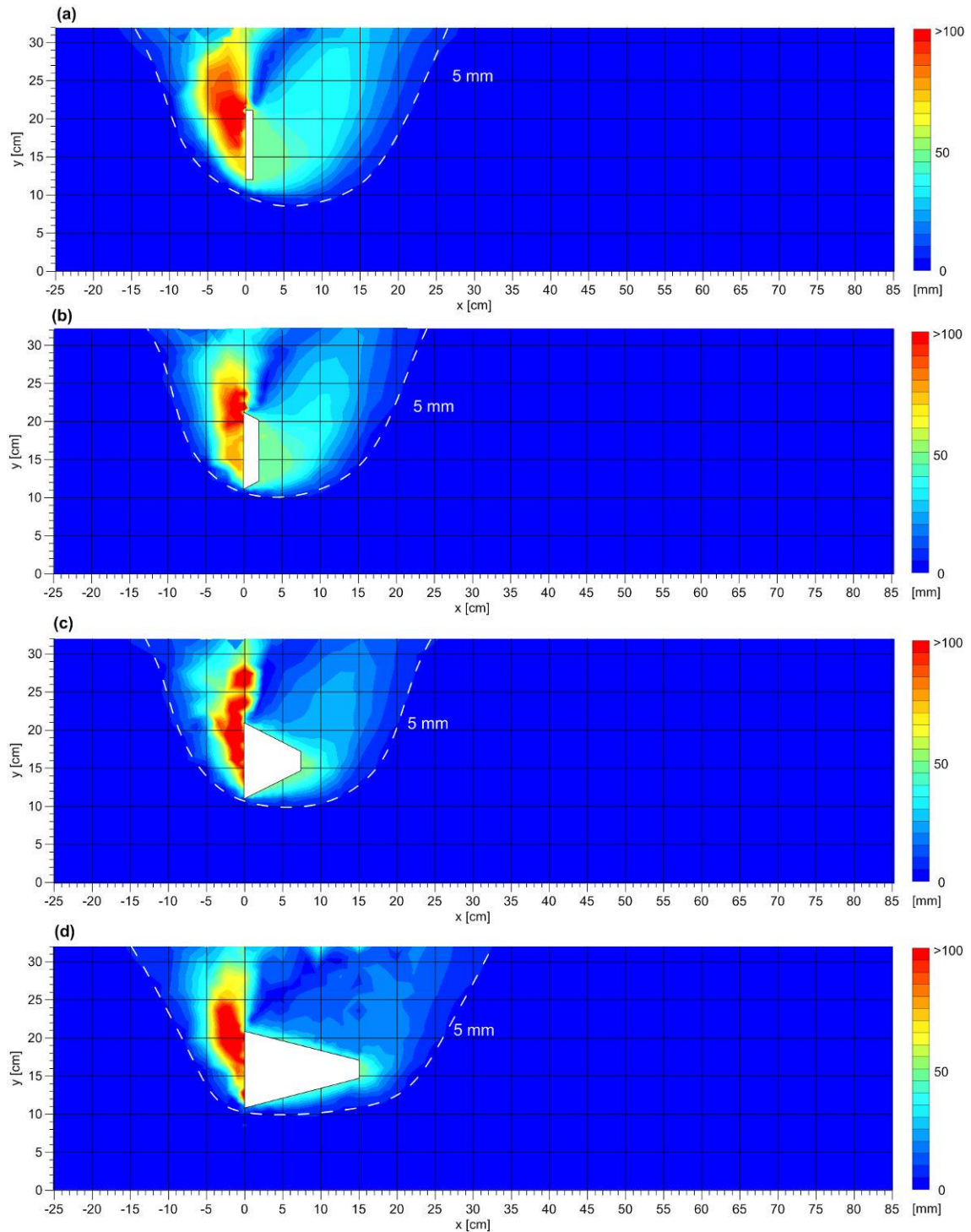


Figure 10 Total displacements in a vertical cross section through the middle of the plate anchor: (a) TS, (b) SFC, (c) MFC, (d) LFC

Table 3 shows a quantitative estimate of the soil area within the dotted lines of Figures 9 and 10. We distinguish the portion which is in front of the anchor ( $A_F$ , for  $x > 0$ ), in a passive state, from the portion which is behind the anchor ( $A_B$ , for  $x < 0$ ), in an active state. The difference  $\Delta A = A_F - A_B$  is related to the pull-out resistance, as it represents the

difference between the zones of soil involved in the passive and active thrusts in front of and behind the plate. To facilitate the comparisons,  $\Delta A$  is normalized over the plate base surface  $A$ . LFC exhibits the wider mobilized soil area, both in horizontal and vertical cross sections, followed by MFC, TS and SFC plates, respectively.

In order to better understand the effect of the three-dimensional shapes, the normalized area difference  $\Delta A/A$  of each shape is compared with the one of the TS, resulting in a mobilization factor  $r_m$ :

$$r_m = \left[ \frac{(A_F - A_B)}{A} \right]_i / \left[ \frac{(A_F - A_B)}{A} \right]_{TS} \quad (2)$$

An estimate of the experimental mobilization factors has been obtained by the analyses of the pictures taken during test set B by means of PIV and absolute image difference technique (Fig. 4) as reported by Bisson (2014). These values are in good agreement with the numerical results. Table 4 summarizes the mobilization factors for the considered shapes and compares the numerical and experimental mobilization factors for the mean vertical plane.

The mobilization factors in Table 4 can be compared to the shape factor  $S_f$  reported in Table 2.  $S_f$  is close to the mobilization factors  $r_{mv}$  and  $r_{mh}$ , thus confirming the existence of a correlation between the pull-out resistance and the size of the volume involved in the resistant mechanisms.

### **4.3 Effect of anchor spacing**

In slope stability applications, plates are used in group as shown in Figure 1b. In this case, the failure surfaces may overlap, thus deteriorating the bearing capacity of the plate compared to the isolated case (Hueckel, 1957). The group efficiency ( $\zeta$ ) is defined as the ratio between the group load capacity ( $Q_g$ ) and the sum of the load capacity of the anchors acting as isolated ( $Q_i$ ) (Geddes, 1996):

$$\zeta = Q_g / \sum Q_i \quad (3)$$

In order to investigate the effect of anchor spacing ( $s$ ) in the limit resistance of a single anchor within the group, further numerical analyses have been performed. This section considers the behaviour of a single element inside an infinite row of anchors, and discusses the effect of  $s$  on  $q_{lim}$  as a function of the shape of the anchor.

Taking advantage of the symmetry of the problem, the geometry of the discretized domain is similar to the one presented in Section 3, only the width ( $w$ ) of the model is modified. The spacing, that is the distance between the centres of two consecutive anchors, is double the model width ( $s=2w$ ). In these analyses the model width is varied between 100 mm and 225 mm, which corresponds to a normalized anchor spacing  $s/B$  ranging between 2 and 5.5.

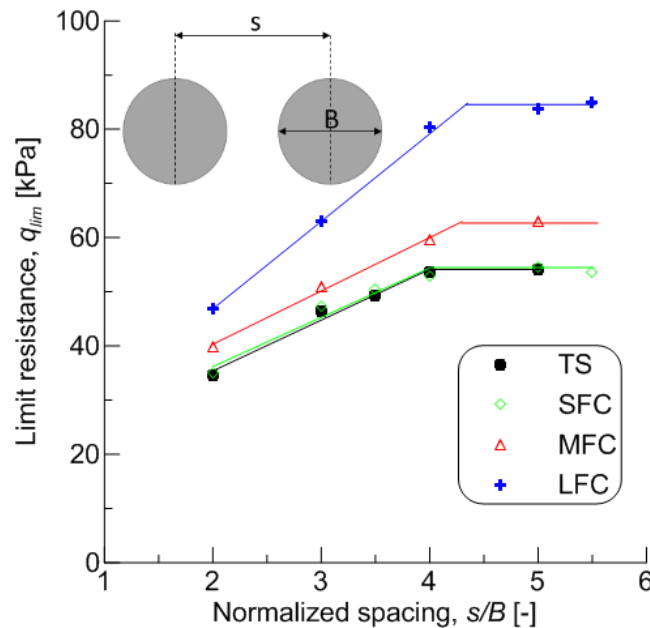


Figure 11 Limit resistance as function of the normalized spacing

Figure 11 shows the limit resistance of the single anchor as function of the normalized spacing for the considered shapes. As  $s$  reduces, correspondingly  $q_{lim}$  also reduces; this means that the efficiency of the anchor group  $\zeta$  increases as the distance between the plates is increased. The trend is approximately linear up to a maximum value, which

corresponds to the free field conditions ( $q_{lim,max}$ ), and then it remains constant. This agrees with previous observations on group efficiency of thin square plate anchors (Geddes, 1996; Hueckel, 1957).

LFC is the shape that provides the highest resistance in free field conditions, followed by MFC; SFC and TS have approximately the same resistance.

The shape of the anchor influences the normalized spacing necessary to reach the maximum limit capacity. LFC and MFC need to be installed with a distance between plates larger than  $4.5-5B$  ( $s/B > 4.5-5$ ) to prevent deterioration of limit capacity due to group effects, i.e. to reach  $\zeta=1$ . In contrast, for SFC and TS the maximum limit resistance is obtained when  $s/B > 4$ . This is a consequence of the size of the pressure bulbs; indeed, as previously noted, LFC and MFC involve a wider volume of soil compared to TS and SFC.

The anchor spacing slightly influences the shape factor; in particular, in free field conditions  $S_f$  reaches the value of 1.57 for LFC and 1.17 for MFC, a little bit larger than the values reported in Table 2.

#### **4.4 Effect of friction angle and Young modulus**

A series of parametric analyses, presented in this section, is carried out to investigate the effect of the soil friction angle and the Young modulus on the limit resistance. The geometry of the numerical model is wide enough to represent the free field conditions, i.e.  $s/B=5$  for TS and  $s/B=5.5$  for LFC and MFC. The interface friction coefficient of the anchor-soil surface is equal to the tangent of the soil friction angle ( $\mu=tan(\varphi)$ ).

Figure 12 shows that the limit capacity increases more than linearly with the friction angle. The results of the SFC are not reported in this figure because they essentially coincide with the results of the TS. The shape factor varies less than 5% within the range

of considered friction angles ( $27^{\circ}$ - $41^{\circ}$ ), thus the dependency of the shape factor on the friction angle can be neglected for most practical applications.

The Young modulus does not significantly modify the limit resistance for various shapes of anchor (Fig. 13). However, in stiffer materials the limit resistance is completely mobilized for smaller displacements.

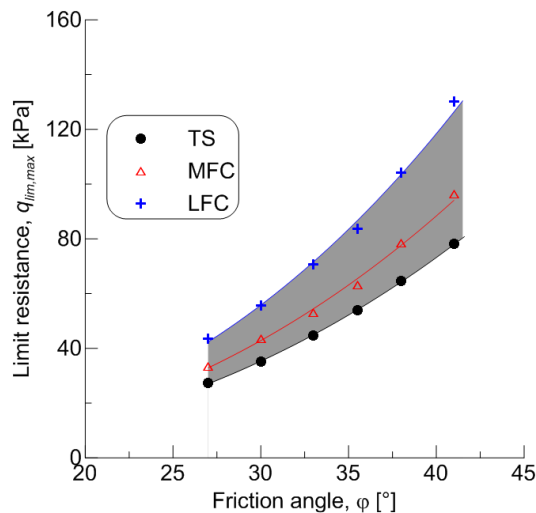


Figure 12 Maximum limit resistance as function of friction angle

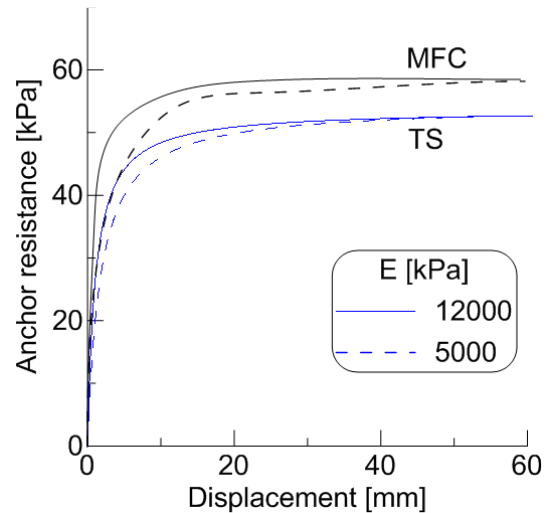


Figure 13 Effect of Young modulus on the displacement-resistance curves.

## 5 Conclusions

This paper investigates the behaviour of shallow plate anchors at large displacements by means of the Material Point Method. Different 3D plate anchor shapes have been considered: thin square, and short, medium-long and long frustocone. The numerical results are in good agreement with experimental pull-out tests.

MFC and LFC show a significantly higher resistance compared to TS. This can be justified by the volume of soil influenced by the movement of the anchor: LFC exhibits the widest volume influence, followed by MFC, TS and SFC, respectively. A shape factor is proposed to correlate the resistance of the 3D shapes to the one of the TS; the latter can be easily calculated by one of the methods proposed in literature, see e.g. B. Das (2013)

and Merifield & Sloan (2006). The shape factor is not significantly influenced by the friction angle and the elastic modulus of soil.

The numerical simulations also considered the behaviour of a plate anchor within a group, showing that the shape slightly influences the normalized spacing necessary to reach the maximum limit capacity. LFC and MFC require larger spacing to prevent group effects ( $s/B > 4.5$ ), compared to SFC and TS ( $s/B > 4$ ). This is in accordance with the size of the pressure bulbs and the volumes of soil involved at large displacements.

Innovative shapes such as cones can be effectively used as plate anchors, providing higher resistances compared to the usual thin square or circular plates; moreover, they can be installed with larger spacing when used in groups. This is particularly interesting in slope stability and slow moving landslide consolidation, where high pull-out resistances at large displacements are required.

The results here presented are obtained verifying the capability of the MPM model to capture the ultimate resistance of anchor plates tested in a 1g physical model at a very small confinement stress. These results must be considered as preliminary results and further tests will be planned, in order to carefully evaluate the effect of dilatancy and stress confinements and therefore reach a more general result.

## **Aknowledgments**

The authors thank Dalla Gassa s.r.l. for the financial support given in this study.

## **References**

- Adrian, R. J. (1991). Particle imaging techniques for experimental fluid mechanics. *Annual Review of Fluid Mechanics*, 23, 261–304.
- Al-Kafaji, I. K. J. (2013). *Formulation of a Dynamic Material Point Method (MPM) for Geomechanical Problems*. Ph.D. thesis, University of Struttgart, Gernay.
- Andersen, S., & Andersen, L. (2010). Analysis of spatial interpolation in the material-

- point method. *Computers & Structures*, 88(7–8), 506–518.
- Atluri, S. N., & Zhu, T. L. (2000). New concepts in meshless methods. *International Journal for Numerical Methods in Engineering*, 47(1–3), 537–556.
- Bardenhagen, S. G., Brackbill, J. U., & Sulsky, D. (2000). The material-point method for granular materials. *Computer Methods in Applied Mechanics and Engineering*, 187(3–4), 529–541.
- Bardenhagen, S. G., Guilkey, J. E., Roessig, K. M., Brackbill, J. U., Witzel, W. M., & Foster, J. C. (2001). An improved contact algorithm for the material point method and application to stress propagation in granular material. *CMES - Computer Modeling in Engineering and Sciences*, 2(4), 509–522.
- Beuth, L. (2012). *Formulation and Application of a Quasi-Static Material Point Method*. Ph.D. thesis, University of Struttgart, Germany.
- Beuth, L., Wiecewski, Z., & Vermeer, P. A. (2011). Solution of quasi-static large-strain problems by the material point method. *International Journal for Numerical and Analytical Methods in Geomechanics*, 35(13), 1451–1465.
- Bisson, A. (2014). *l'ancoraggio flottante SIRIVE per la stabilizzazione di movimenti franosi*. PhD thesis, University of Padua, Italy.
- Bisson, A., & Cola, S. (2014). Ancoraggi flottanti per la stabilizzazione di movimenti franosi lenti. In *La geotecnica nella difesa del territorio e delle infrastrutture dalle calamità naturali, Vol.2* (pp. 327–334). Baveno, Italy: AGI.
- Bisson, A., Cola, S., Tessari, G., & Floris, M. (2015). Floating Anchors in Landslide Stabilization: The Cortiana Case in North-Eastern Italy. In *Engineering Geology for Society and Territory - Vol. 2*. (pp. 2083–2087). Zurich: Springer International Publishing.
- Ceccato, F. (2014). *Study of large deformation geomechanical problems with the Material Point Method*. Ph.D. thesis, University of Padua, Italy.
- Ceccato, F., Beuth, L., & Simonini, P. (2016). Analysis of Piezocone Penetration under Different Drainage Conditions with the Two-Phase Material Point Method. *Journal of Geotechnical and Geoenvironmental Engineering*, 142(12), 4016066.
- Ceccato, F., Beuth, L., & Simonini, P. (2017). Adhesive contact algorithm for MPM and

- its application to the simulation of cone penetration in clay. In *Procedia Engineering* (pp. 182–188).
- Ceccato, F., Beuth, L., Vermeer, P. A., & Simonini, P. (2016). Two-phase Material Point Method applied to the study of cone penetration. *Computers and Geotechnics*, *80*, 440–452.
- Ceccato, F., & Simonini, P. (2016). Numerical study of partially drained penetration and pore pressure dissipation in piezocone test. *Acta Geotechnica*, *12*(1), 195–209.
- Cruden, D. M., & Varnes, D. J. (1996). Landslides: investigation and mitigation. Chapter 3-Landslide types and processes. In *Transportation research board special report 247* (pp. 36–75). Transportation Research Board.
- Das, B. (1975). Pullout resistance of vertical anchors. *Journal of the Geotechnical Engineering Division*, *101*(1), 87–91.
- Das, B. (2013). *Earth anchors* (Second edi). J. Ross Publishing.
- Das, B. M., & Seely, G. R. (1975). Load-displacement relationship for vertical anchor plates. *Journal of the Geotechnical Engineering Division*, *101*(7), 711–715.
- Detournay, C., & Dzik, E. (2006). Nodal Mixed Discretization for tetrahedral elements. In *Proceedings of the 4th International FLAC Symposium on Numerical Modeling in Geomechanics*. Madrid.
- Donea, J., & Huerta, A. (2004). Arbitrary Lagrangian–Eulerian methods. *Encyclopedia of Computational Mechanics*, (1969), 1–38.
- Fern, E. J., de Lange, D. A., Zwanenburg, C., Teunissen, J. A. M., Rohe, A., & Soga, K. (2016). Experimental and Numerical investigations of dyke failures involving soft materials. *Engineering Geology*.
- Fern, E. J., & Soga, K. (2016). The Role of Constitutive Models in MPM Simulations of Granular Column Collapses. *Acta Geotechnica*, *11*(3), 659–678.
- Gabrieli, F., Cola, S., & Calvetti, F. (2009). Use of an up-scaled DEM model for analysing the behaviour of a shallow foundation on a model slope. *Geomechanics and Geoengineering*, *4*(2), 109–122.
- Geddes, J. D. (1996). Plate anchor groups pulled vertically in sand. *Journal of Geotechnical Engineering*, *122*(July), 509–516.

- Gottardi, G., & Simonini, P. (2003). The viscoplastic behaviour of a geogridreinforced model wall. *Geosynthetics International*, 10, 34–46.
- Grabe, J., Qiu, G., & Wu, L. (2015). Numerical simulation of the penetration process of ship anchors in sand. *Geotechnik*, 38(1), 36–45.
- Hu, Y., & Randolph, M. F. (1998). A practical numerical approach for large deformation problems in soils. *International Journal for Numerical and Analytical Method in Geomechanics*, 22(5), 327–350.
- Hueckel, S. (1957). Model tests on anchoring capacity of vertical and inclined plates. In *Proceedings of the 4th international conference on soil mechanics and foundations engineering* (pp. 203–206). London.
- Jassim, I., Stolle, D., & Vermeer, P. (2013). Two-phase dynamic analysis by material point method. *International Journal for Numerical and Analytical Methods in Geomechanicsnumerical and Analytical Methods in Geomechanics*, 37, 2502–2522.
- Kumar Soundararajan, K. (2015). *Multi-scale multiphase modelling of granular flows*. PhD Thesis, University of Cambridge.
- Lim, L. (2014). On the application of the material point method for offshore foundations. In M. Hicks, Brinkgreve, & A. Rohe (Eds.), *Numerical Methods in Geotechnical Engineering* (pp. 253–258). Taylor and Francis group.
- Love, E., & Sulsky, D. (2005). *An energy consistent material point method for dynamic finite deformation plasticity*. *International journal for numerical methods ...* Albuquerque, New Mexico.
- Mahmoodzadeh, H., & Randolph, M. (2014). Penetrometer Testing: Effect of Partial Consolidation on Subsequent Dissipation Response. *Journal of Geotechnical and Geoenvironmental Engineering*, 140(6), 1–12.
- Merifield, R. S., & Sloan, S. W. (2006). The ultimate pullout capacity of anchors in frictional soils. *Canadian Geotechnical Journal*, 43(8), 852–868.
- Neely, W. J., Stuart, J. G., & Graham, J. (1973). Failure loads of vertical anchor plates in sand. *Journal of the Soil Mechanics and Foundations Division*, 99(9), 669–685.
- Noh, W. (1994). CEL: a time-dependent, two-space-dimensional, coupled Eulerian–Lagrangian code. *Fundam Methods Hydrodynam*, (13), 117–179.

- Ovesen, N. K. & Stromann, H. (1972). Design methods for vertical anchor slabs in sand. In *Performance of Earth and Earth-Supported Structures* (pp. 1481–1500). New York, USA: ASCE.
- Phuong, N. T. V., van Tol, A. F., Elkadi, A. S. K., & Rohe, A. (2016). Numerical investigation of pile installation effects in sand using material point method. *Computers and Geotechnics*, *73*, 58–71.
- Qiu, G., & Grabe, J. (2011). Explicit modeling of cone and strip footing penetration under drained and undrained conditions using a visco-hypoplastic model. *Geotechnik*, *34*(3), 205–217.
- Qiu, G., & Henke, S. (2011). Controlled installation of spudcan foundations on loose sand overlying weak clay. *Marine Structures*, *24*(4), 528–550.
- Qiu, G., Henke, S., & Grabe, J. (2011). Application of a Coupled Eulerian–Lagrangian approach on geomechanical problems involving large deformations. *Computers and Geotechnics*, *38*(1), 30–39.
- Rosin, P. L., & Ellis, T. (1995). Image difference threshold strategies and shadow detection. In David Pycock (Ed.), *Proceedings of the British Machine Conference* (pp. 347–356).
- Simonini, P. (1987). *Fondazioni superficiali su sabbia: modellazione teorica e sperimentale*. PhD thesis, University of Padua, Italy.
- Simonini, P. (1996). A finite element approach to the strength of granular soils reinforced with geosynthetics. In *Proceedings of the International Symposium on Earth Reinforcement* (pp. 675–680).
- Soga, K., Alonso, E., Yerro, A., Kumar, K., & Bandara, S. (2016). Trends in large-deformation analysis of landslide mass movements with particular emphasis on the material point method. *Géotechnique*, *66*(3), 248–273.
- Steffen, M., Kirby, R. M., & Berzins, M. (2008). Analysis and reduction of quadrature errors in the material point method (MPM). *International Journal for Numerical Methods in Engineering*, *76*, 922–9448.
- Sulsky, D., Chen, Z., & Schreyer, H. L. (1994). A particle method for hystory-dependent materials. *Computer Methods in Applied Mechanics and Engineering*, *118*(1–2),

179–196.

Sulsky, D., Zhou, S.-J., & Schreyer, H. L. (1995). Application of a particle-in-cell method to solid mechanics. *Computer Physics Communications*, 87(1–2), 236–252.

Tian, Y., Cassidy, M. J., Randolph, M. F., Wang, D., & Gaudin, C. (2014). A simple implementation of RITSS and its application in large deformation analysis. *Computers and Geotechnics*, 56, 160–167. 1

Vermeer, P. A., Yuan, Y., Beuth, L., & Bonnier, P. (2009). Application of interface elements with the Material Point Method. In *Proceedings of the 18th International Conference on Computer Methods in Mechanics* (pp. 477–478). Zielona Gora, Poland.

White, D. J., Take, W. a., & Bolton, M. D. (2003). Soil deformation measurement using particle image velocimetry ( PIV ) and photogrammetry. *Geotechnique*, 53(7), 619–631.

Yerro, A. (2015). *MPM modelling of landslides in brittle and unsaturated soils*. Ph.D thesis, Univesitat Politecnica de Catalunya, Spain.

Yerro, A., Alonso, E. E., & Pinyol, N. M. (2016). Run-out of landslides in brittle soils. *Computers and Geotechnics and Geotechnics*, 1–13.

## **Appendix A: Basic concepts of the Material Point Method**

MPM applies a continuum approach, which means that the governing equations of motions are derived from the equations of conservation of mass, momentum, energy and the stress-strain relation. A discretized form of these equations is obtained by applying the Galerking method and approximating the trial and test functions by means of nodal basis function like in FEM. However, in contrast to ordinary Updated Lagrangian FEM, with MPM the mesh does not store any permanent information and does not deform with the body. Indeed, all the information of the continuum (velocity, acceleration, stress, strain, state variables and material parameters) is stored at the material points (MP) and mapped to/from the nodes of the mesh each time step by means of interpolation functions. Large deformations are modelled by MP moving through the computational mesh. This

Appendix summarizes only the main features of the MPM solution scheme. For further information, the reader may refer to the pioneering work of Sulsky and co-workers (Bardenhagen, Brackbill, & Sulsky, 2000; Love & Sulsky, 2005; Sulsky et al., 1994).

Let us consider the strong form of the momentum balance equation for a 1-phase material:

$$\rho \mathbf{a} = \text{div}(\boldsymbol{\sigma}) + \rho \mathbf{g} \quad (4)$$

where  $\rho$  = material density,  $\mathbf{a}$  = acceleration,  $\mathbf{g}$  = gravity vector,  $\boldsymbol{\sigma}$  = stress tensor.

This equation is discretized in space with the Galerking method and solved in time with an explicit Euler-Cromer scheme:

$$\mathbf{a}^t = \mathbf{M}^{t,-1}(\mathbf{F}_{ext}^t - \mathbf{F}_{int}^t) \quad (5)$$

where  $\mathbf{M}^t$  is the lumped mass matrix at time  $t$ ,  $\mathbf{a}^t$  is the nodal acceleration,  $\mathbf{F}_{int}^t$  is the vector of nodal internal forces,  $\mathbf{F}_{ext}^t$  is the vector of nodal external forces (let us assume for simplicity that only gravity is applied). The terms on the right hand side are assembled by means of material point quadrature over the body domain  $\Omega$ :

$$\mathbf{F}_{int}^t = \int_{\Omega} \mathbf{B}^{t,T} \boldsymbol{\sigma}^t d\Omega = \sum_{p=1}^{n_p} V_p^t \mathbf{B}_p^{t,T} \boldsymbol{\sigma}_p^t \quad (6)$$

$$\mathbf{F}_{grav} = \int_{\Omega} \mathbf{N}^T \boldsymbol{\rho} \mathbf{g} dV = \sum_{p=1}^{n_p} \mathbf{N}_p^{t,T} m_p \mathbf{g} = \sum_{p=1}^{n_p} \mathbf{N}_p^{t,T} \mathbf{f}_p^{grav} \quad (7)$$

where the subscript  $p$  indicates that the quantity is computed at the MP location,  $\mathbf{N}$  is the matrix of nodal shape functions,  $\mathbf{B}$  contains the derivatives of the shape functions,  $V_p$  is the volume (quadrature weight) of the MP,  $m_p$  is the mass,  $\boldsymbol{\sigma}_p$  is the stress,  $\mathbf{f}_p^{grav}$  is the gravity force. Note that material point integration is applied in MPM; in contrast, Gauss point integration is commonly performed in FEM, which is one of the main differences between these methods.

Once the nodal acceleration is obtained by solving equation (5), the acceleration, velocity, strains and stresses at the MP are computed. Finally, the position of the MP is updated and eventually a new element is assigned to those points that crossed element boundaries.

The solution algorithm for each time increment can be summarized as follows:

- (1) Assemble the system of governing equations
- (2) Solve Equation (5) for the nodal acceleration
- (3) Compute the velocity of MP
- (4) Compute nodal incremental displacement and derive strains of MP
- (5) Apply the constitutive relation to find stresses of MP
- (6) Update volume, density and other state variables of MP
- (7) Compute displacement of MP and update their position
- (8) Eventually modify the mesh and assign MP to new elements

The mapping of a generic quantity from the nodes to the MPs is done by means of the shape functions. For example, the updated MP velocity at step (3) is computed as:

$$\mathbf{v}_p^{t+\Delta t} = \mathbf{v}_p^t + \sum_n^{N_n} \Delta t N_n(\boldsymbol{\xi}_p) \mathbf{a}_n^t \quad (8)$$

where the summation runs over the  $N_n$  nodes of the element that contains the MP  $p$ ,  $\boldsymbol{\xi}_p$  is the local coordinate of the MP,  $\mathbf{a}_n^t$  is the acceleration of node  $n$  at time  $t$ ,  $\Delta t$  is the time increment.

The software applied in this study is an enhanced version of the above presented original MPM, which implements specific procedures to mitigate problems of volumetric locking and grid-crossing errors that cause stress oscillations.

The finite element discretization adopted in this study uses low order tetrahedral elements, which can give volumetric-locking issues in slightly-compressible materials. This is mitigated with the Nodal Mixed Discretization technique (Detournay & Dzik, 2006), which consists in weakening the incompressibility constraint by incorporating information of surrounding elements. First, the nodal strain rates are computed as a weighted average of the volumetric strain rates of the adjacent elements. Second, the enhanced strain rates for each element is calculated by averaging its nodal values. Further details can be found in Jassim, Stolle, & Vermeer (2013).

The movement of MP across element boundaries is known to cause noise in the solution (Andersen & Andersen, 2010; Steffen et al., 2008). With the used enhanced MPM variant, Gauss integration is applied in fully filled elements (elements in which the sum of the volumes of the contained MPs is greater than 90% of the element volume) (L Beuth, Wicowski, & Vermeer, 2011). This approach proved to reduce the noise significantly (Al-Kafaji, 2013).

## **Appendix B: Contact algorithm**

MPM is able to model non-slip contact between bodies without any special contact formulation; indeed, at the contact, the bodies' velocities are identical because they belong to the same vector field, thus no interpenetration or sliding is allowed. In order to simulate frictional sliding, a specific algorithm must be implemented.

There are several possibilities for taking into account the soil-structure interaction such as the use of interface elements (Vermeer, Yuan, Beuth, & Bonnier, 2009), or level-set based contact algorithms (Lim, 2014), but one of the most popular approaches within the MPM software is the one proposed by Bardenhagen et al. (2001). This algorithm is briefly described in the following paragraph; further details can be found in the original publication and in Ceccato et al. (2017), or Al-Kafaji (2013).

Let us consider two bodies, labelled A and B, in contact. The nodal velocities of the single body ( $\mathbf{v}_A$ ,  $\mathbf{v}_B$ ) and the nodal velocity of the system of bodies ( $\mathbf{v}_S$ ) are predicted by solving the respective momentum equations. A node is identified as a contact node if the velocity of the single body differs from the one of the combined system. If so, the algorithm checks if the bodies are approaching or separating. If they are separating, there is no need for correction and the velocities correspond to the single body velocities. Otherwise, the sliding condition is checked.

The sliding condition is based on the contact forces. If the tangential contact force is lower than the maximum value allowed by the contact law, the bodies stick to each other and the velocity is equal to the system velocity. If the bodies are sliding with respect to each other, then the single body velocity is corrected in such a way that no interpenetration occurs and the contact force respects the Coulomb friction law, i.e. the maximum tangential force is proportional to the normal force through a friction coefficient ( $\mu$ ).

The corrected nodal velocity at the contact node  $k$ , is calculated as:

$$\tilde{\mathbf{v}}_{k,A} = \mathbf{v}_{k,A} - [(\mathbf{v}_{k,A} - \mathbf{v}_{k,S}) \cdot \mathbf{n}_{k,A}] \mathbf{n}_{k,A} + [(\mathbf{v}_{k,A} - \mathbf{v}_{k,S}) \cdot \mathbf{n}_{k,A}] \mu \mathbf{t}_k \quad (9)$$

where  $\mathbf{v}_{k,A}$  and  $\mathbf{v}_{k,S}$  are predicted velocities for the single body and the coupled system respectively,  $\mathbf{n}_{k,A}$  is the outward normal vector to body A at the node,  $\mathbf{t}_k$  is the tangential vector,  $\mu$  is the friction coefficient.

The second term on the right-hand side represents the correction for the normal component in order to ensure no interpenetration. The third term represents the correction for the tangential component in order to respect the contact law. The correction for nodal velocity is applied before updating the MP quantities (velocity, position, strain, stress etc.).